Journal of Materials Chemistry C

ROYAL SOCIETY OF CHEMISTRY

PAPER

View Article Online
View Journal | View Issue

Cite this: J. Mater. Chem. C, 2022, 10, 6857

The structural evolution, optical gap, and thermoelectric properties of the $RbPb_2Br_5$ layered halide, prepared by mechanochemistry†

Carmen Abia,[ab] Carlos A. López,[ac] Javier Gainza,[a] João Elias F. S. Rodrigues,[ad] Mateus M. Ferrer,[e] N. M. Nemes,[af] Oscar J. Dura,[g] José L. Martínez,[a] María T. Fernández-Díaz,[b] Consuelo Álvarez-Galván,[h] Gergely Németh,[i] Katalin Kamarás,[i] François Fauth[j] and José A. Alonso*[a]

Rubidium di-lead pentabromide, $RbPb_2Br_5$, belongs to a family of layered lead-containing halides, with the common formula APb_2X_5 (where A = K, Rb, Cs; X = Cl, Br). The optical properties of $RbPb_2Br_5$ and rare-earth doped specimens are promising as low-phonon energy materials for tunable middle infrared and long-wavelength infrared laser sources, with suitable stability and resistance to wet conditions. In contrast to $CsPb_2Br_5$, the Rb counterpart has been barely studied and deserves further attention. Up to now, there have been no experimental reports on the transport properties such as the electronic conductivity, Seebeck coefficient or thermal transport. We describe here that this material can be prepared by ball milling in a straightforward way, yielding specimens with superior crystallinity. A structural investigation using synchrotron X-ray powder diffraction (SXRD) data combined with neutron powder diffraction (NPD) in a wide temperature range, from 15 to 573 K, was essential to evaluate the thermal evolution and to determine the Debye constants, yielding information on the relative Rb–Br and Pb–Br chemical bonds. In combination with DSC and TG measurements, no phase transitions were observed. Furthermore, an analysis of SXRD and NPD data (XRD-NPD) at room temperature reveals the directions of electron lone pair of Pb^{2+} ions lead atoms: its stereochemical effect is obvious in the $[PbBr_8]$ octahedral distortions. Diffuse reflectance UV-Vis spectroscopy yields an optical gap of 3.36 eV, close to that determined for a single-crystal material. Photoluminescence measurements indicate a lack of overlap between the excitation and emission spectra, due to the considerable Stokes shift, which prohibits self-absorption and thus enables applications in photovoltaics and biomedicine. The experimental information about the chemical bonds and band gap was studied *via* first-principles calculations. A maximum positive Seebeck coefficient of 3200 $\mu V\ K^{-1}$ is obtained at 560 K, which is one order of magnitude higher than those reported for other halide perovskites.

Received 16th February 2022,
Accepted 29th March 2022

DOI: 10.1039/d2tc00653g

rsc.li/materials-c

Introduction

Since 2012, hybrid halide perovskites containing both organic and inorganic cations have attracted attention for photovoltaic applications in view of their high power conversion efficiency, which reaches values above 22%, close to silicon-based solar cells.[1] However, totally inorganic perovskite derivatives also depict interesting optical properties with a great potential for

[a] Instituto de Ciencia de Materiales de Madrid, CSIC, Cantoblanco, 28049 Madrid, Spain. E-mail: ja.alonso@icmm.csic.es, calopez@unsl.edu.ar
[b] Institut Laue Langevin, BP 156X, F-38042 Grenoble, France
[c] Instituto de Investigación en Tecnología Química (UNSL-CONICET) and Facultad de Química, Bioquímica y Farmacia, Almirante Brown 1455, (5700) San Luis, Argentina
[d] European Synchrotron Radiation Facility (ESRF), 71 Avenue des Martyrs, 38000 Grenoble, France
[e] CCAF, PPGCEM/CDTec, Federal University of Pelotas, 96010-610 Pelotas, Rio Grande do Sul, Brazil
[f] Departamento de Física de Materiales, Universidad Complutense de Madrid, E-28040 Madrid, Spain
[g] Departamento de Física Aplicada, Universidad de Castilla-La Mancha, Ciudad Real, E-13071, Spain
[h] Instituto de Catálisis y Petroleoquímica, CSIC, Cantoblanco, 28049 Madrid, Spain
[i] Institute for Solid State Physics and Optics, Wigner Research Centre for Physics, P. O. Box 49, Budapest, H-1525, Hungary
[j] CELLS–ALBA synchrotron Light Facility, Cerdanyola del Valles, Barcelona, E-08290, Spain

† Electronic supplementary information (ESI) available. See DOI: https://doi.org/10.1039/d2tc00653g

solar cell applications; it is the case of the cubic $CsPbI_3$, due to its narrow bandgap of 1.73 eV.[2] Such compounds are less sensitive to ambient oxygen and water, yet have a high fluorescence quantum yield. The main hindrance here for its widespread use resides on the difficult stabilization of the cubic α-$CsPbI_3$ phase at room temperature, which undergoes a phase change to the undesirable orthorhombic (δ) phase (non-perovskite).[3]

A recognized strategy to improve the stability in $CsPbI_3$ concerns a partial or complete substitution of I by Br, which leads to a more stable orthorhombic $CsPbBr_3$ perovskite.[4–12] Bromide also acts by changing the bandgap according to its content. Such a perovskite shows a high and constant photoresponse, being also more stable than $CsPbI_3$ to ambient atmosphere and humidity. However, $CsPbBr_3$ presents a higher bandgap (2.3 eV), that would hinder its application in solar cell devices, although allowing its use in optoelectronic systems.[13]

Very recently, interesting alternative strategies have been developed to achieve higher photoefficiencies in these halide perovskites, which include structural ordering and different topologies for the octahedral arrangements in the case of $Cs_3Bi_2Br_9$[14–19] and $CsPb_2Br_5$.[20–24] From a topological view, the former has 0D dimensionality (*i.e.* no connection between octahedra) and the latter a 2D one, instead of the classical 3D arrangement of $CsPbBr_3$ with corner-sharing [$PbBr_6$] units. $Cs_3Bi_2Br_9$ exhibits good stability, while $CsPb_2Br_5$ has added interest due to its layered structure for thin film fabrication and application in photovoltaic devices.[24–26]

Rubidium di-lead pentabromide, $RbPb_2Br_5$, belongs to this fascinating family of layered lead-containing halides, with the common formula APb_2X_5 (where A = K, Rb, Cs; X = Cl, Br). The crystal growth and emission properties of $RbPb_2Br_5$ were described in the nineties,[27] and the electronic structure and optical properties were estimated more recently,[28] finding this halide and rare-earth doped specimens to be promising as low-phonon energy materials for tunable middle infrared (mid-IR) and long-wavelength infrared (long-wave-IR) laser sources for remote sensing and other applications.[29,30] In contrast to $CsPb_2Br_5$, the Rb counterpart has been barely studied and it deserves further attention. Despite the mentioned antecedents, up to now there are no experimental reports on the transport properties such as the electronic conductivity, Seebeck coefficient or thermal transport.

In this work, we have succeeded in the synthesis of a well-crystallized $RbPb_2Br_5$ specimen using a solvent-free mechano-chemical method, enabling an accurate structural study from synchrotron X-ray diffraction (SXRD) and neutron powder diffraction (NPD) in a wide temperature range. $RbPb_2Br_5$ is tetragonal, defined in the space group *I*4/*mcm* (#140),[31] and does not experience any phase transition below the melting point.[32] In this paper, we derive the Debye temperatures from the atomic displacement factors, yielding interesting trends for the relative strength of Rb–Br *vs.* Pb–Br chemical bonds, complemented by DFT-based calculations. An optical gap of 3.36 eV is determined from UV-Vis spectra. The characterization of this ball-milled specimen is complemented by DSC measurements and scanning microscopy. Transport properties reveal a Seebeck coefficient of 13 000 $\mu V\ K^{-1}$ at 440 K.

Experimental methods

$RbPb_2Br_5$ was synthesized in the polycrystalline form by mechano-chemical synthesis (ball milling) from stoichiometric amounts of $PbBr_2$ and RbBr. The total mass of reactants was 1.5 g, which were weighed and mixed with 20 zirconia balls (5 mm diameter) in a N_2-filled glove-box. The reaction was carried out in a Retsch PM100 mill for 4 h at 450 rpm, in a sealed zirconia-lined jar in an N_2 atmosphere. Laboratory XRD patterns were collected in a Bruker D5 diffractometer with Cu-K_α (λ = 1.5418 Å) radiation. The thermal evolution of the crystallographic structure was studied by SXRD, at room temperature (30 °C) and above (100, 200, 300, 400, and 500 °C). SXRD patterns were collected in high angular resolution mode (the so-called MAD set-up) on the MSPD diffractometer in an ALBA synchrotron in Barcelona, Spain, selecting an incident beam with 38 keV energy, λ = 0.325760 Å.[33] The sample was contained in a 0.5 mm diameter quartz capillary that was rotating during the data acquisition. NPD patterns were sequentially collected using a D20 instrument, a high-flux diffractometer in the ILL reactor (Grenoble) with a wavelength of 1.540 Å, in the 15–396 K temperature interval, with a 5 K step and 30 min collection time for each diagram. NPD and SXRD patterns were analyzed using the Rietveld method using the *FullProf* program.[34,35] Differential scanning calorimetry (DSC) measurements were carried out in the range 130 K to 520 K in a Mettler TA3000 system equipped with a DSC-30 unit. The heating and cooling rates were 10 K min^{-1}, using about 70 mg of sample in each run. Field-effect Scanning Electron Microscopy (FE-SEM) images were obtained on a FEI-Nova microscope, with an acceleration potential of 5 kV, coupled to an energy-dispersive X-ray spectrometer (EDX), working at an acceleration voltage of 18 kV and 60 s of acquisition time. The optical diffuse reflectance spectrum was measured at room temperature using a UV-Vis spectrophotometer Varian Cary 5000. Photoluminescence spectra were measured on a HORIBA Jobin Yvon Fluorolog-3 spectrofluorometer (Nanolog). Solid powder samples were placed between two CaF_2 plates and illuminated by a 450 W Xenon lamp at 45° incidence. The emission was detected using an R928P photomultiplier tube.

The resulting powder obtained from ball milling was pressed into a pellet by hand using a cold press, while the sample was kept at room temperature throughout the whole process. The resistivity and thermal conductivity were measured in the pressed pellet, which was cut into a bar shape using a diamond saw to measure the Seebeck coefficient. The Seebeck coefficient was obtained by simultaneously measuring drop voltages across the sample and a constantan reference wire with an electrometer (Keithley 6517B) and nanovoltmeter (Keithley 2182A) under vacuum (10^{-3} mbar). Electrical conductivity measurements were carried out by using a HP 4284 LCR analyzer in the 20 Hz–1 MHz frequency range, with an applied

ac voltage of 0.5 V. Electrodes were deposited on the pellet's flat surfaces by applying silver paste. The total thermal conductivity was calculated from the thermal diffusivity (α) using a Linseis LFA 1000 equipment, using the laser-flash technique. Both faces of the sample were covered with a thin graphite layer to ensure black body emissivity. The thermal conductivity (κ) was determined using $\kappa = \alpha c_p d$, where c_p is the specific heat and d is the sample density.

Computational methods

A theoretical model based on Density Functional Theory (DFT) using the CRYSTAL17 package was performed to support the chemical environment of the system.[36] The HSE06 hybrid functional was used since it generates similar results to the structural and electronic data of the experimental system.[37] The atomic basis set was defined using Triple-Zeta valence with the polarization Gaussian basis (POB-TZVP) sets developed by Laun and co-workers.[38] The Coulomb and exchange series in the CRYSTAL17 package is controlled by five thresholds (overlap and penetration for Coulomb integrals, the overlap for HF exchange integrals, and the pseudo-overlap), where the values defined for the calculations were 8, 8, 8, 8, and 16 (10^{-8}, 10^{-8}, 10^{-8}, 10^{-8}, and 10^{-16}). The two shirking factors (Pack–Monkhorst method for the grid of k points and Gilat net for the sampling) were set to 6 and 6, respectively. In the structure optimization step, the gradient components and nuclear displacements were adjusted with tolerances on their root mean square of 0.0003 and 0.0012 a.u., respectively. The chemical environment was evaluated using "Quantum Theory: Atoms in Molecules" (QTAIM) using TOPOND, a program that is part of the crystal package.[39]

Results and discussion

Initial characterization

The sample was obtained as a white microcrystalline powder; the laboratory XRD pattern at room temperature exhibits a tetragonal symmetry, in agreement with previous reports, indexable in the space group *I*4/*mcm*. It belongs to the $(NH_4)Pb_2Br_5$ structural type.[40] The crystal structure was preliminary refined in this structural model from laboratory XRD data, as displayed in Fig. S1 (ESI†), obtaining as unit-cell parameters a = 8.4562(4) Å and c = 14.584(1) Å.

Fig. 1a and b illustrate the DSC curves (in the heating and cooling runs) and the TG curve, respectively. No significant events are identified in the calorimetric curve in the 130–520 K temperature range, while the weight low above 600 °C indicated full decomposition of the sample, by Br loss.

Fig. 1c and d illustrates some FE-SEM images, giving insight into the microstructure of this product, synthesized by ball milling. An overall view with low magnification (18 500×) shows irregular-shaped clusters of particles of different sizes (Fig. 1c). However, in a large magnification view (100 000×), Fig. 1d unveils that they are indeed formed by tiny nanoparticles of uneven form, with a typical size of 140–170 nm, which are grown during the ball milling process. EDX analysis coupled to the FE-SEM images yields an atomic composition

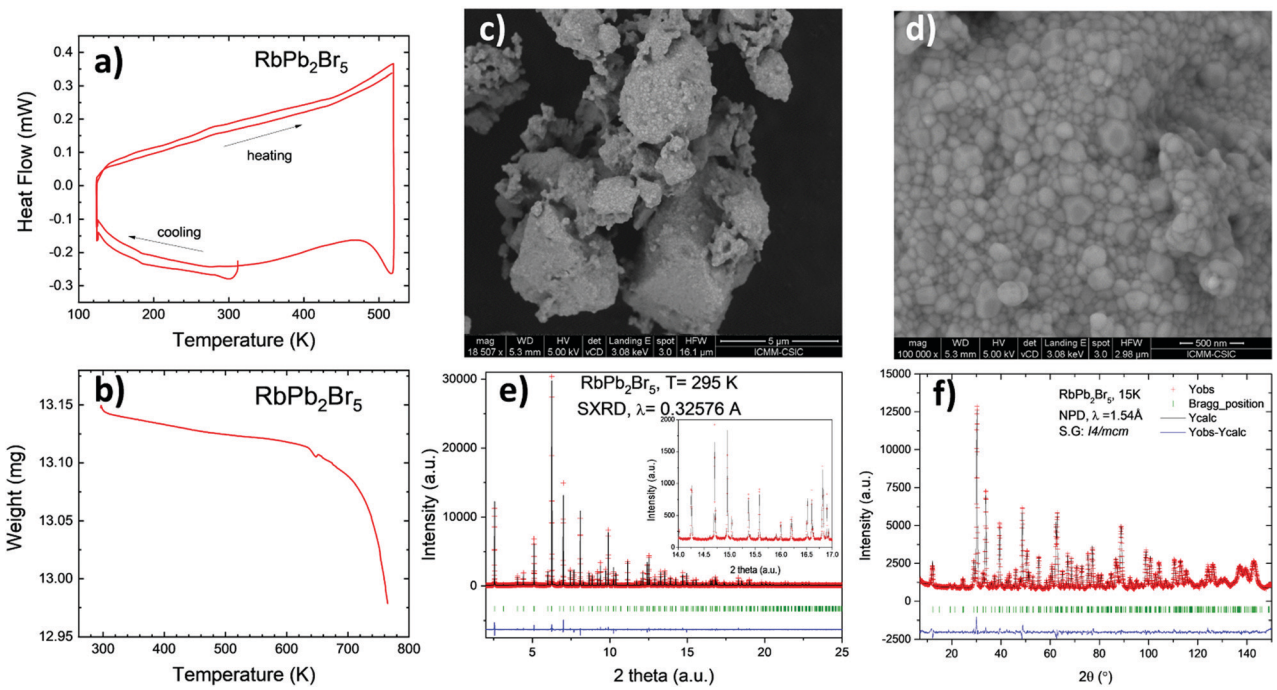

Fig. 1 (a) First and second cycle of DSC curves. (b) TG curve, showing weight loss upon decomposition of the sample above 600 °C. FE-SEM images with (c) 18 500× and (d) 100 000× magnification. (e) Observed (crosses), calculated (full line) and difference (bottom) Rietveld profiles for $RbPb_2Br_5$ from SXRD data at room temperature. The inset highlights the quality of the fit at high diffraction angles. (f) Rietveld plot from NPD data at 15 K.

close to 1 : 1 : 3 for the Rb:Pb:I ratio. A typical EDX spectrum is included in Fig. S2 in the ESI;† other SEM images are included in Fig. S3 (ESI†).

The synchrotron pattern collected at room temperature confirms the tetragonal symmetry in the *I*4/*mcm* space group (#140). The Rb^{1+} and Pb^{2+} ions are located in 4*a* (0,0,1/4) and 8*h* (*x*,*x* + 0.5,0) Wyckoff sites; Br1 and Br2, the two types of bromine, are located at 4*c* (0,0,0) and at 16*l* (*x*,*y*,*z*) respectively. The quality of the final refinement using this model is illustrated in Fig. 1e, and the main crystallographic results are listed in Table 1. Two views of the crystal structure are shown in Fig. 2a and b. The unit cell parameters refined at room temperature, of a = 8.44479(4) Å, c = 14.59265(7) Å, V = 1040.667(8) Å^3, are comparable to those reported, a = 8.4455(1) Å, c = 14.5916(3) Å, V = 1040.77 Å^3.[40] The structure consists of layers of [$PbBr_8$] polyhedra sharing edges and triangular faces, allowing for short Pb–Pb distances of 4.009(1) Å at RT across these faces. The layers are connected by Rb^{1+} ions, in ten-fold coordination with eight shorter (3.605(1) Å) and two longer (3.648 Å) Rb–Br bond lengths. In fact, the [$PbBr_8$] polyhedra are strongly distorted, as derived from the stereochemical effect of the Pb^{2+} lone electron pair.

The crystal structure in the 15–396 K interval was additionally investigated from NPD data collected in the D20 diffractometer (ILL). No structural changes were observed, other than the expected thermal contraction of the unit-cell parameters upon cooling down the sample (Fig. 2d–f). The volume has a thermal expansion with temperature of 0.1198(12) Å^3 K^{-1}, while the *a* and *c* unit cell parameters increase as 2.93(2) × 10^{-4} Å K^{-1} and 6.85(8) × 10^{-4} Å K^{-1}, respectively. The moderate absorption of neutrons by the heavy Rb and Pb atoms was suitable to study the thermal variation of the displacement factors in all the temperature range. The quality of the NPD Rietveld fit is illustrated for the 15 K pattern, included in Fig. 1f.

An analysis of SXRD and NPD data (XRD-NPD) was useful to obtain additional information about the electron lone pair of Pb^{2+} ions. This procedure uses the structural information refined from NPD data to perform difference Fourier syntheses using SXRD data, which contain information on the electron density in the crystal, as was reported earlier.[41] The results are plotted in Fig. 2c, where the difference electron density is shown as a yellow isosurface. This picture reveals a non-negligible density up and down Pb^{2+} ions along the *c*-axis. We assume that the 6s^2 electrons are delocalized between both *c*-axis directions. This delocalized character of the Pb^{2+} electron lobes does not yield a net polarization, in agreement with the centrosymmetric nature of the crystal structure.

Table 1 Crystallographic parameters for $RbPb_2Br_5$ refined from SXRD data at room temperature

Atom		*x*	*y*	*z*	U_{iso}	Occ
Rb	4*a*	0.16783 (9)	0.66783 (9)	0	0.0290 (3)	1
Pb	8*h*	0	0	0.25	0.0333 (8)	1
Br1	4*c*	0	0	0	0.0261 (8)	1
Br2	16*l*	0.6557 (1)	0.1557 (1)	0.1351 (1)	0.0301 (4)	1

R_p: 7.66%; R_{wp}: 9.29%; R_{exp}: 5.76%; χ^2 : 2.72; R_{Bragg}: 5.15%. System: tetragonal, space group: *I*4/*mcm*, Z = 4. Unit-cell parameters: a = 8.44479(4) Å, c = 14.59265(7) Å and V = 1040.67(1) Å^3.

Mean-square displacements

The mean-square displacements (MSDs) of the atomic species in $RbPb_2Br_5$ (Rb, Pb, Br1, and Br2) were derived as isotropic displacement parameters (U_{eq}, units of Å^2) in the temperature range from 15 up to 573 K. The temperature dependence of the MSDs extracted from NPD (15–396 K) and SXRD (300–573 K) can be modelled in the framework of the Debye model,[42,43] *i.e.*

$$U_{eq} = d_S^2 + \frac{3\hbar^2 T}{m k_B \theta_D^2}\left[\frac{T}{\theta_D}\int_0^{\theta_D/T}\frac{x}{e^x - 1}dx + \frac{\theta_D}{4T}\right]$$

where, d_S^2 concerns the intrinsic disorder, θ_D is the Debye temperature, m the atom's mass, k_B the Boltzmann constant, $\hbar$ the reduced Planck constant, and T the absolute temperature. Rb showed an intrinsic disorder of ~3.5 × 10^{-4} Å^2, while such parameters were slightly below zero (~10^{-4} Å^2) for Pb, Br1, and Br2. Therefore, d_S^2 was fixed to zero for those elements. Fig. 3 depicts the temperature dependence of the MSDs for Rb, Pb, Br1, and Br2 and their respective fittings using the Debye model. From them, the Debye temperature values were derived, as follows: Rb (113 K), Pb (84 K), Br1 (141 K), and Br2 (129 K). The Debye temperature can provide information on the bonding stiffness by means of the harmonic one-particle potential OPP model,[44,45] in which the harmonic potential depends on θ_D^2. Here, the force constant is evaluated by

$$k = \frac{m k_B^2 \theta_D^2}{3\hbar^2}$$

where, k is the force constant in units of eV Å^{-2}. The as-obtained k values are the following: 0.65(5) eV Å^{-2} for Rb, 0.86(3) eV Å^{-2} for Pb, 0.93(8) eV Å^{-2} for Br1, and 0.79(3) eV Å^{-2} for Br2. It means that the bonding nature of Rb–Br and Pb–Br are similar, but the latter one is slightly more rigid than the former one. It may indicate a tendency for a covalency in the Pb–Br bond pair. Based on the low values of Debye temperatures, typically below 150 K, $RbPb_2Br_5$ must have ultra-low values of thermal conductivity below 1 W m^{-1} K^{-1}.

Topological analysis of the main Bond Critical Points (BCPs) of the theoretical model for $RbPb_2Br_5$ was performed in order to evaluate the above experimental estimates. The BCP parameters are listed in Table 2.

According to the parameters in Table 2, all the bonds present low values of ρ and positive values of $\nabla^2\rho$, which indicate a preponderant ionic character. On the other hand, the parameters between Rb–Br and Pb–Br bonds have some crucial differences. The H parameter of BCPs attributed to Rb–Br is positive, being negative for those attributed to the Pb–Br bonds. In addition, the $|V|/G$ ratio of Rb–Br is less than 1, while in the Pb–Br BCPs it is greater than 1. These parameters of Pb–Br BCPs indicate that such bonds fall into a transient class showing a relevant covalent contribution.[46] Therefore, the theoretical data exhibited a good agreement with the results

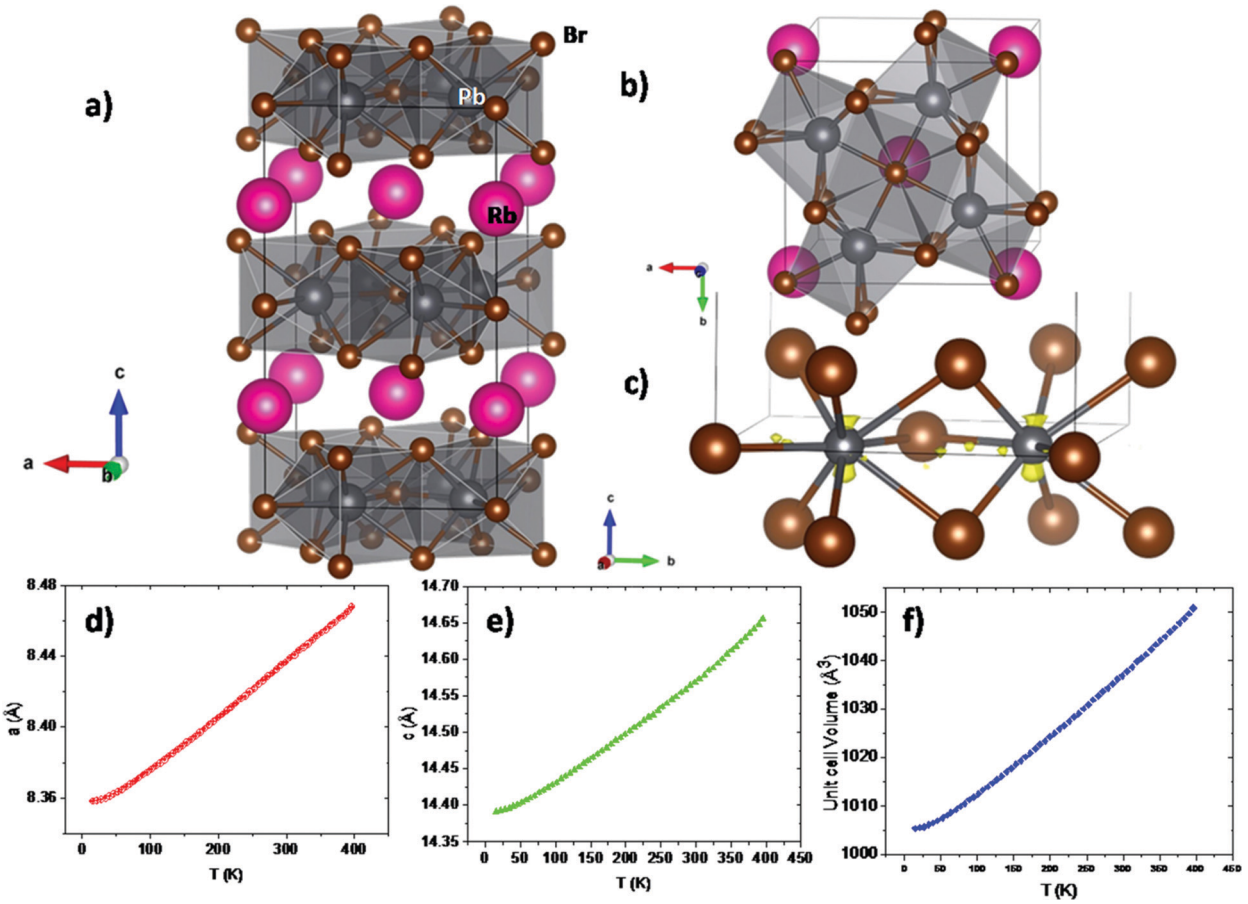

Fig. 2 (a) View of the layered crystal structure of $RbPb_2Br_5$. The layers are constituted by [$PbBr_8$] polyhedra sharing edges and faces, with Rb atoms between the layers (b) close up showing the connection between [$PbBr_8$] polyhedra. There are short Pb–Pb distances across the triangular faces of the polyhedra. (c) Two [$PbBr_8$] coordination polyhedra connected by a common face; the Pb^{2+} electron lone pair has been located from XRD-NPD data, as shown by the yellow lobes of electron density. (d, e and f) are plots of the thermal evolution of the *a*, *c* and *V* parameters, respectively.

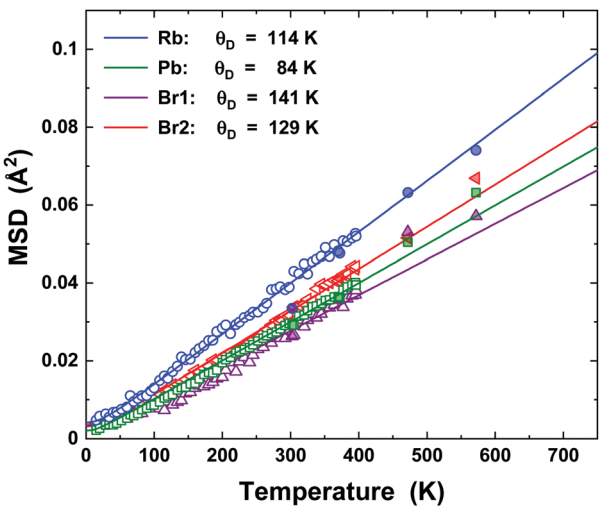

Fig. 3 Temperature dependence of U_{eq} (MSD) for Rb, Pb, and Br1, and Br2 atoms. Open symbols represent the MSD values extracted from the sequential Rietveld refinement (NPD), while filled ones were obtained from SXRD. The lines denote the best fits to the experimental data using the Debye model. Standard deviations are smaller than the size of the symbols.

Table 2 Bond critical points (BCPs) parameters for the $RbPb_2Br_5$ halide: electron density (ρ), Laplacian of electron density ($\nabla^2\rho$), virial field density (*V*), Lagrangian kinetic energy density (*G*), and total energy (*H*)

Bond	Distance (Å)	ρ ($\times10^{-3}$)	$\nabla^2\rho$ ($\times10^{-2}$)	G ($\times10^{-3}$)	V ($\times10^{-3}$)	H ($\times10^{-3}$)	$\lvert V\rvert/G$
Rb–Br	3.68	6.20	2.22	4.36	−3.17	1.19	0.73
Pb–Br	2.94	36.0	7.28	21.3	−24.4	−3.11	1.14
Pb–Br	3.16	22.1	4.94	12.5	−12.7	−0.20	1.02
Pb–Br	3.32	18.1	3.75	9.49	−9.60	−0.10	1.01

obtained by Debye analysis, where the Rb–Br bond has a greater ionic character than the Pb–Br bond.

The Laplacian of the electronic density isolines at the (100) and (001) planes are depicted in Fig. 4. The bond Rb–Br along the (100) plane with isolines close to Rb atoms are very isolated, probably due to their predominant ionic character. The bond Pb–Br presented along the (001) plane has a distance of 3.16 Å. It is interesting to highlight the difference of the isoline profiles between Rb–Br and Pb–Br bonds. The isolines of Pb along the (001) plane show a certain entanglement degree with the Br

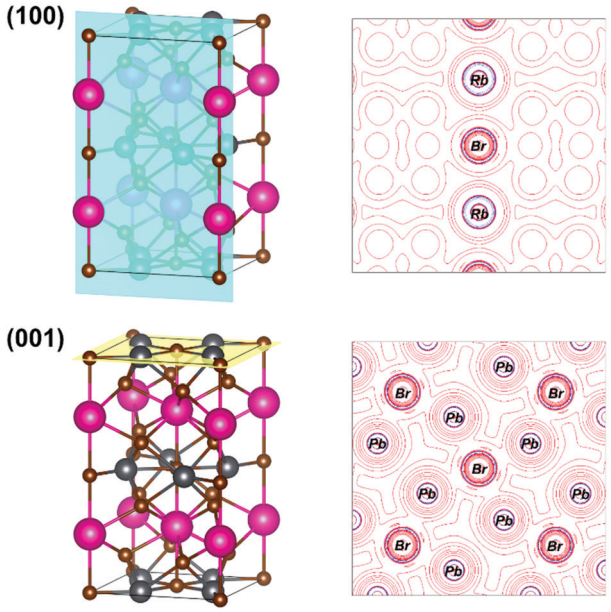

Fig. 4 (100) and (001) planes and their respective Laplacians of electronic density (isolines) of the $RbPb_2Br_5$ halide model.

isolines, which is due to the contribution of covalence of such bonds. It is important to make it clear that the assignment of covalence is a relative comparison with the Rb–Br bond, since both bonds have an ionic character.

Thermoelectric properties

Fig. 5 shows the transport thermoelectric properties measured near room temperature: resistivity (Fig. 5a), Seebeck coefficient (Fig. 5b), and power factor (Fig. 5c). The resistivity is higher than 10^7 Ω m at 310 K, a really high value that is quite far from being competitive with other materials, such as some halide perovskites.[47] However, this value is close to the $\sim 3.3 \times 10^6$ Ω m resistivity reported for undoped $MAPbBr_3$ single crystals.[48] The resistivity also decreases with temperature, which is caused by the activation of minority carriers. The activation energy for the carriers in $RbPb_2Br_5$, calculated from the measured electrical conductivity, is 512 meV (Fig. S4, ESI†).

The Seebeck coefficient strongly varies with temperature, adopting a negative value immediately above room temperature (*e.g.* $-13\,000$ μV K^{-1} at 440 K) and then changing its sign and reaching $S = 3{,}200$ μV K^{-1} at 560 K, and then becoming negative again at 620 K. The maximum positive value is about one order of magnitude higher than the Seebeck coefficients reported for other halide perovskites like $CsSnBr_3$ and hybrid perovskites like $MAPbBr_3$.[47,48] Even these high Seebeck coefficient values are not enough to achieve a great power factor ($S^2\sigma$), which remains low due to the high resistivity.

The thermal conductivity κ (Fig. 6a) is, on the other hand, lower than that reported for other halide and hybrid perovskites,[47,48] and remains always below 0.26 W m^{-1} K at all the measured temperatures, from 300 K up to 573 K. Such a value has intrinsic origin based on low Debye temperatures for Rb, Pb, and Br. We can combine these values in a zT figure of merit (Fig. 6b), defined as $zT = S^2\sigma T/\kappa$, that yields $zT = 1 \times 10^{-6}$ at 570 K, which is low compared with the state-of-the-art thermoelectric materials, but is comparable to other reported values for halide perovskites, like Bi-doped $MAPbBr_3$, which shows a zT of 1.8×10^{-6} at 293 K.[48]

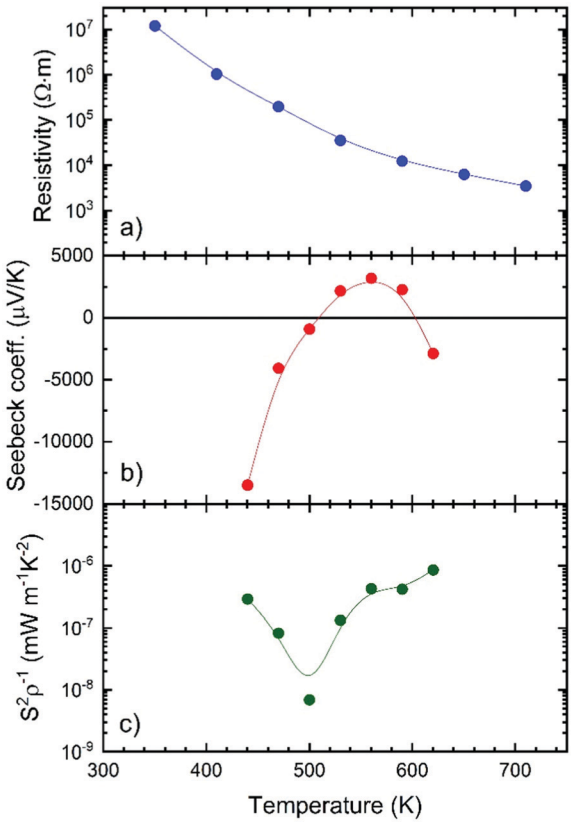

Fig. 5 (a) Electrical resistivity, (b) Seebeck coefficient, and (c) power factor of $RbPb_2Br_5$.

Optical gap by UV-Vis spectra and emission by photoluminescence spectra

The absorption capacity of the $RbPb_2Br_5$ powder was first investigated by diffuse reflectance UV/Vis spectroscopy. Fig. 7a depicts the optical absorption coefficient related to the Kubelka–Munk function [$F(R) = (1 - R)^2/2R$, R being the reflectance *versus* wavelength in eV]. The band gap has been calculated by extrapolating the linear region to the abscissa. The value obtained for $RbPb_2Br_5$ ($\sim$3.36 eV) is typical for this material, and close to those reported in the literature for a single crystal material, of 3.42–3.47 eV.[49] The band structure and the density of states (DOS) of the $RbPb_2Br_5$ halide were evaluated from the theoretical model, as shown in Fig. S5a (ESI†). The band structure (a) shows an indirect transition $N \rightarrow \Gamma$ of 3.55 eV, a value close to the experimental band gap. The state contributions in each band is displayed in Fig. S5b (ESI†). The valence band is mainly constituted by the density of states related to Br atoms as well as the conduction band mainly by Pb states.

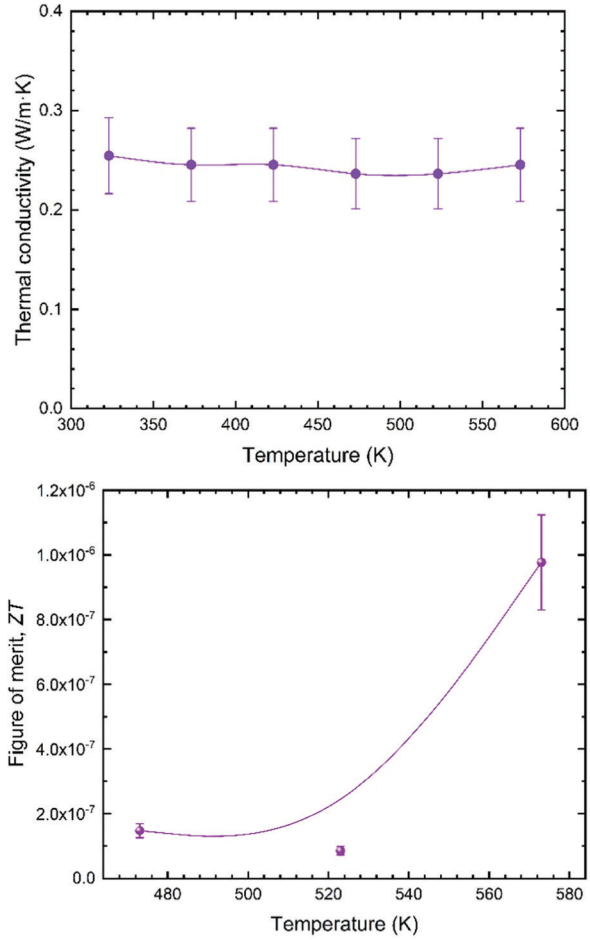

Fig. 6 (a) Thermal conductivity of $RbPb_2Br_5$. (b) Thermoelectric figure of merit for the $RbPb_2Br_5$ halide, with a guiding curve to show its tendency.

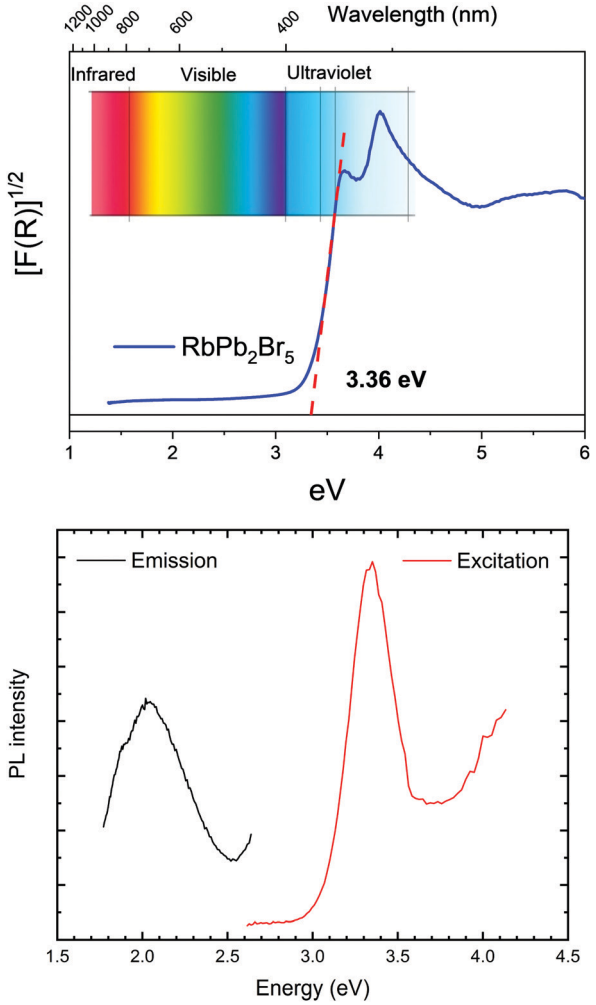

Fig. 7 (a) Kubelka–Munk (KM) transformed diffuse reflectance spectrum of $RbPb_2Br_5$ halide. (b) Photoluminescence by emission and excitation.

Afterwards, the emission spectrum was determined with 350 nm (3.54 eV, slightly above the band gap) excitation wavelength, obtaining maximum intensity at 600 nm (2.06 eV). The excitation spectrum was then measured by setting the detection monochromator to 600 nm and tuning the excitation wavelength between 300 and 500 nm. The excitation spectrum (red curve in Fig. 7b) follows the absorption determined by diffuse reflectance (Fig. 7a). The lack of overlap between the excitation and emission spectra (black curve in Fig. 7b), due to the considerable Stokes shift, prohibits self-absorption and thus enables applications in photovoltaics and biomedicine. A similar large Stokes shift was reported in $RbSn_2Br_5$.[50]

Conclusions

The $RbPb_2Br_5$ halide has been successfully prepared as a well-crystallized powder by mechano-chemical synthesis in an inert atmosphere. The crystal structure evolution has been revisited from high angular resolution SXRD and NPD data. The structure contains disported $[PbBr_8]$ polyhedra, where the lone electron pair of Pb^{2+} has been located using XRD and NPD techniques revealing that the $6s^2$ electrons are delocalized up and down of Pb^{2+} ions along the *c*-axis. The evolution of the displacement factors has been analysed in the framework of the Debye model, determining the Debye temperatures for the different atoms, as well as the relative stiffness of the Rb–Br *vs.* Pb–Br pair bonds, following the harmonic one-particle potential model. The bonding natures of Rb–Br and Pb–Br bonds are similar, but the Pb–Br bond is slightly more rigid than the former. It may indicate a tendency for a greater covalence in the Pb–Br bond pair. The thermoelectric properties are appealing, regarding a large Seebeck coefficient and a low thermal conductivity, although the large electrical resistivity leads to negligible figure of merit values. The optical band gap of 3.36 eV of this ball-milled specimen is similar to that reported for single crystal samples, being corroborated by *ab initio* calculations (indirect transition of 3.55 eV). The lack of overlap between the excitation and emission photoluminescence spectra enables applications in photovoltaics and biomedicine.

Author contributions

C. A., J. E. F. S. R. and C. A. G. and prepared the sample; C. A., M. T. F. D., J. A. A. and C. A. L. collected and analysed the

structural NPD data; J. A. A., C. A. L. and F. F. collected and analysed the SXRD data; J. G., N. M. N., O. J. D. and J. L. M. carried out the thermoelectric measurements; J. E. F. S. R. and M. M. F. performed the Debye analysis and *ab initio* calculations; C. A. G. carried out the optical measurements; G. N. and K. K. carried out photoluminescence measurements; all the authors participated in the discussion of results and redaction of the article.

Conflicts of interest

There are no conflicts to declare.

Acknowledgements

The Spanish Ministry of Science, Innovation and Universities supported this work through grant MAT2017-84496-R. The authors wish to express their gratitude to ALBA technical staff for making the facilities available for the Synchrotron X-ray powder diffraction experiment number 2020094572. J. G. thanks MICINN for granting the contract PRE2018-083398. C. A. is thankful for financial support from the Institut Laue-Langevin through the DA/SRH/GRI/AS/19-214 contract. G. N. and K. K. thank National Research, Development and Innovation Office of Hungary through Grant no. NKFIH FK-138411.

References

1 W. S. Yang, B.-W. Park, E. H. Jung, N. J. Jeon, Y. C. Kim, D. U. Lee, S. S. Shin, J. Seo, E. K. Kim, J. H. Noh and S. Il Seok, *Science*, 2017, **356**, 1376–1379.
2 D. B. Straus, S. Guo and R. J. Cava, *J. Am. Chem. Soc.*, 2019, **141**, 11435–11439.
3 Z. Chen, L. Dong, H. Tang, Y. Yu, L. Ye and J. Zang, *CrystEngComm*, 2019, **21**, 1389–1396.
4 J. Peng, C. Q. Xia, Y. Xu, R. Li, L. Cui, J. K. Clegg, L. M. Herz, M. B. Johnston and Q. Lin, *Nat. Commun.*, 2021, **12**, 1531.
5 X. Li, W. Cai, H. Guan, S. Zhao, S. Cao, C. Chen, M. Liu and Z. Zang, *Chem. Eng. J.*, 2021, **419**, 129551.
6 L. Peng, A. Dutta, R. Xie, W. Yang and N. Pradhan, *ACS Energy Lett.*, 2018, **3**, 2014–2020.
7 B. J. Bohn, Y. Tong, M. Gramlich, M. L. Lai, M. Döblinger, K. Wang, R. L. Z. Hoye, P. Müller-Buschbaum, S. D. Stranks, A. S. Urban, L. Polavarapu and J. Feldmann, *Nano Lett.*, 2018, **18**, 5231–5238.
8 Y. Gao, L. Zhao, Q. Shang, Y. Zhong, Z. Liu, J. Chen, Z. Zhang, J. Shi, W. Du, Y. Zhang, S. Chen, P. Gao, X. Liu, X. Wang and Q. Zhang, *Adv. Mater.*, 2018, **30**, 1801805.
9 J. Song, J. Li, L. Xu, J. Li, F. Zhang, B. Han, Q. Shan and H. Zeng, *Adv. Mater.*, 2018, **30**, 1800764.
10 J. Duan, Y. Zhao, X. Yang, Y. Wang, B. He and Q. Tang, *Adv. Energy Mater.*, 2018, **8**, 1802346.
11 Y. He, L. Matei, H. J. Jung, K. M. McCall, M. Chen, C. C. Stoumpos, Z. Liu, J. A. Peters, D. Y. Chung, B. W. Wessels, M. R. Wasielewski, V. P. Dravid, A. Burger and M. G. Kanatzidis, *Nat. Commun.*, 2018, **9**, 1609.
12 C. A. López, C. Abia, M. C. Alvarez-Galván, B.-K. Hong, M. V. Martínez-Huerta, F. Serrano-Sánchez, F. Carrascoso, A. Castellanos-Gómez, M. T. Fernández-Díaz and J. A. Alonso, *ACS Omega*, 2020, **5**, 5931–5938.
13 P. Acharyya, K. Kundu and K. Biswas, *Nanoscale*, 2020, **12**, 21094–21117.
14 Y. Zhu, J. Zhu, H. Song, J. Huang, Z. Lu and G. Pan, *J. Rare Earths*, 2021, **39**, 374–379.
15 Z. Ji, Y. Liu, W. Li, C. Zhao and W. Mai, *Sci. Bull.*, 2020, **65**, 1371–1379.
16 B. Yang and K. Han, *Acc. Chem. Res.*, 2019, **52**, 3188–3198.
17 M. Leng, Y. Yang, K. Zeng, Z. Chen, Z. Tan, S. Li, J. Li, B. Xu, D. Li, M. P. Hautzinger, Y. Fu, T. Zhai, L. Xu, G. Niu, S. Jin and J. Tang, *Adv. Funct. Mater.*, 2018, **28**, 1704446.
18 B. Yang, J. Chen, F. Hong, X. Mao, K. Zheng, S. Yang, Y. Li, T. Pullerits, W. Deng and K. Han, *Angew. Chem., Int. Ed.*, 2017, **56**, 12471–12475.
19 C. W. M. Timmermans and G. Blasse, *Phys. Status Solidi*, 1981, **106**, 647–655.
20 R. Wang, Z. Li, S. Li, P. Wang, J. Xiu, G. Wei, H. Liu, N. Jiang, Y. Liu and M. Zhong, *ACS Appl. Mater. Interfaces*, 2020, **12**, 41919–41931.
21 Y.-Q. Zhou, J. Xu, J.-B. Liu and B.-X. Liu, *J. Phys. Chem. Lett.*, 2019, **10**, 6118–6123.
22 C. Wang, Y. Wang, X. Su, V. G. Hadjiev, S. Dai, Z. Qin, H. A. Calderon Benavides, Y. Ni, Q. Li, J. Jian, M. K. Alam, H. Wang, F. C. Robles Hernandez, Y. Yao, S. Chen, Q. Yu, G. Feng, Z. Wang and J. Bao, *Adv. Mater.*, 2019, **31**, 1902492.
23 P. Acharyya, P. Pal, P. K. Samanta, A. Sarkar, S. K. Pati and K. Biswas, *Nanoscale*, 2019, **11**, 4001–4007.
24 J. Duan, Y. Zhao, B. He and Q. Tang, *Angew. Chem.*, 2018, **130**, 3849–3853.
25 G. Tong, T. Chen, H. Li, W. Song, Y. Chang, J. Liu, L. Yu, J. Xu, Y. Qi and Y. Jiang, *Sol. RRL*, 2019, **3**, 1900030.
26 X. Tang, S. Han, Z. Zu, W. Hu, D. Zhou, J. Du, Z. Hu, S. Li and Z. Zang, *Front. Phys.*, 2017, **5**, 69.
27 K. Nitsch, V. Hamplová, M. Nikl, K. Polák and M. Rodová, *Chem. Phys. Lett.*, 1996, **258**, 518–522.
28 A. A. Lavrentyev, B. V. Gabrelian, V. T. Vu, N. M. Denysyuk, P. N. Shkumat, A. Y. Tarasova, L. I. Isaenko and O. Y. Khyzhun, *J. Phys. Chem. Solids*, 2016, **91**, 25–33.
29 K. Rademaker, E. Heumann, G. Huber, S. A. Payne, W. F. Krupke, L. I. Isaenko and A. Burger, *Opt. Lett.*, 2005, **30**, 729.
30 K. Rademaker, W. F. Krupke, R. H. Page, S. A. Payne, K. Petermann, G. Huber, A. P. Yelisseyev, L. I. Isaenko, U. N. Roy, A. Burger, K. C. Mandal and K. Nitsch, *J. Opt. Soc. Am. B*, 2004, **21**, 2117.
31 O. Nazarenko, M. R. Kotyrba, M. Wörle, E. Cuervo-Reyes, S. Yakunin and M. V. Kovalenko, *Inorg. Chem.*, 2017, **56**, 11552–11564.
32 S. V. Mel'nikova, L. I. Isaenko, V. M. Pashkov and I. V. Pevnev, *Phys. Solid State*, 2006, **48**, 2152–2156.
33 F. Fauth, R. Boer, F. Gil-Ortiz, C. Popescu, O. Vallcorba, I. Peral, D. Fullà, J. Benach and J. Juanhuix, *Eur. Phys. J. Plus*, 2015, **130**, 160.
34 H. M. Rietveld, *J. Appl. Crystallogr.*, 1969, **2**, 65–71.

35 J. Rodríguez-Carvajal, *Phys. B*, 1993, **192**, 55–69.
36 R. Dovesi, A. Erba, R. Orlando, C. M. Zicovich-Wilson, B. Civalleri, L. Maschio, M. Rérat, S. Casassa, J. Baima, S. Salustro and B. Kirtman, *Wiley Interdiscip. Rev.: Comput. Mol. Sci.*, 2018, **8**, e1360.
37 A. V. Krukau, O. A. Vydrov, A. F. Izmaylov and G. E. Scuseria, *J. Chem. Phys.*, 2006, **125**, 224106.
38 J. Laun, D. Vilela Oliveira and T. Bredow, *J. Comput. Chem.*, 2018, **39**, 1285–1290.
39 S. Casassa, A. Erba, J. Baima and R. Orlando, *J. Comput. Chem.*, 2015, **36**, 1940–1946.
40 D. Becker and H. P. Beck, *Z. Anorg. Allg. Chem.*, 2004, **630**, 1924–1932.
41 C. A. López, E. Bâati, M. T. Fernández-Díaz, F. O. Saouma, J. I. Jang and J. A. Alonso, *J. Solid State Chem.*, 2019, **276**, 122–127.
42 J. L. Feldman and G. K. Horton, *Phys. Rev.*, 1963, **132**, 644–647.
43 J.-L. Mi, M. Christensen, E. Nishibori and B. B. Iversen, *Phys. Rev. B: Condens. Matter Mater. Phys.*, 2011, **84**, 064114.
44 B. T. M. Willis and A. W. Pryor, *Thermal Vibrations in Crystallography*, Cambridge University Press, 1975, vol. 50.
45 A. Nakatsuka, A. Yoshiasa, K. Fujiwara and O. Ohtaka, *J. Mineral. Petrol. Sci.*, 2018, **113**, 280–285.
46 C. Gatti, V. R. Saunders and C. Roetti, *J. Chem. Phys.*, 1994, **101**, 10686–10696.
47 H. Xie, S. Hao, J. Bao, T. J. Slade, G. J. Snyder, C. Wolverton and M. G. Kanatzidis, *J. Am. Chem. Soc.*, 2020, **142**, 9553–9563.
48 W. Tang, J. Zhang, S. Ratnasingham, F. Liscio, K. Chen, T. Liu, K. Wan, E. S. Galindez, E. Bilotti, M. Reece, M. Baxendale, S. Milita, M. A. McLachlan, L. Su and O. Fenwick, *J. Mater. Chem. A*, 2020, **8**, 13594–13599.
49 A. Y. Tarasova, L. I. Isaenko, V. G. Kesler, V. M. Pashkov, A. P. Yelisseyev, N. M. Denysyuk and O. Y. Khyzhun, *J. Phys. Chem. Solids*, 2012, **73**, 674–682.
50 K. Kundu, P. Dutta, P. Acharyya and K. Biswas, *Mater. Res. Bull.*, 2021, **140**, 111339.